Available online at www.sciencedirect.com

ScienceDirect

Nuclear Engineering and Design 237 (2007) 2292–2301

Nuclear Engineering and Design

www.elsevier.com/locate/nucengdes

Development of thermal fatigue damage in 1CrMoV rotor steel

S.R. Holdsworth [a,*], E. Mazza [a,1], L. Binda [a], L. Ripamonti [b]

[a] Empa, Swiss Federal Laboratories for Materials Testing & Research, Switzerland
[b] ALSTOM (Switzerland) Ltd., Switzerland

Received 3 November 2006; received in revised form 2 May 2007; accepted 6 May 2007

Abstract

Crack initiation endurances have been determined for a 1CrMoV rotor steel in uniaxial service cycle thermo-mechanical fatigue (TMF) tests formulated to simulate a range of steam turbine start cycles with a maximum temperature of 565 °C. The experimental details for these TMF tests are described.

Post test inspection has been employed to characterise the associated thermal fatigue damage mechanisms for the steel which are observed to be dependent on the magnitude of the thermal transient in the TMF cycle.

The lowest resistance to thermal fatigue damage development occurs in these tests when the conditions determine that the rate of creep damage accumulation below the surface exceeds the rate of fatigue crack development at the surface.

1. Introduction

Critical locations in steam turbine rotors may be subject to the combined accumulation of cyclic damage arising from strain transients generated during start-up and shut-down, and creep damage resulting from primary (directly applied) and secondary (self equilibrating) stresses during operation. Traditionally, the risk of thermal fatigue cracking at such locations has been assessed using the results from isothermal tests conducted at (or close to) the peak operating temperature, e.g. Timo (1969), Mayer and Tremmel (1979), Dawson (1989) and Härkegard (1992). 1CrMoV steel has been used widely for HP/IP steam turbine rotors operating at temperatures up to ~565 °C and there is an extensive knowledge base covering isothermally determined LCF, creep and cyclic/hold properties of the steel, e.g. Bhongbhibhat (1979), Thomas and Dawson (1980), Miller et al. (1984), Bicego et al. (1988) and Holdsworth (1996).

The development of creep-fatigue damage in isothermal cyclic/hold tests on 1CrMoV steel depends on temperature, strain range, strain rate, hold time, and the creep ductility of the material, Thomas and Dawson (1980), Miller et al. (1984), Bicego et al. (1988). In the absence of a significant hold time (and/or at relatively high strain rates), crack initiation and growth is fatigue-dominated, even at temperatures of ~538–565 °C (Fig. 1a). With increasing hold time (and/or decreasing strain rate) and decreasing strain range, the creep damage condition within the testpiece becomes increasingly influential, to the limit beyond which crack development becomes fully creep-dominated (Fig. 1b). At intermediate hold times and strain ranges, fatigue cracking interacts with creep damage developing consequentially or simultaneously resulting in accelerated crack growth (Fig. 1c and d). The extent of any interaction increases with decreasing creep ductility, Miller et al. (1984).

As part of an activity to examine the effectiveness of state-of-the-art creep-fatigue assessment procedures, a series of service cycle thermo-mechanical (TMF) tests were carried out to provide a collation of well characterised deformation and endurance data, for a single heat of 1CrMoV rotor steel, gathered under anisothermal conditions intended to be representative of operation in service, i.e. Colombo et al. (2003), Masserey et al. (2003), Holdsworth et al. (2004) and Mazza et al. (2004a,b). An integral part of these investigations was the post test examination of TMF testpieces to fully characterise their damage condition with respect to the material mechanical property data to which it related. The main purpose of this action was to mechanistically

* Corresponding author at: Empa, Swiss Federal Laboratories for Materials Testing & Research, Laboratory for Mechanics for Modelling & Simulation, Überlandstrasse 129, CH-8600 Dübendorf, Switzerland. Tel.: +41 44 823 4732.
E-mail address: stuart.holdsworth@empa.ch (S.R. Holdsworth).
[1] Also at: ETH Zurich, Institute of Mechanical Systems, CH-8092 Zurich, Switzerland.

0029-5493/$ – see front matter © 2007 Elsevier B.V. All rights reserved.
doi:10.1016/j.nucengdes.2007.05.002

Nomenclature

A	constant in Norton–Bailey law (Eq. (4))
C	constant in yield function (Eq. (3))
d, Δd	testpiece gauge section diameter, local change in diameter at end of test
FEA	finite element analysis
HΔT	high ΔT (cycle)
IΔT	intermediate ΔT (cycle)
J_2	second invariant of the deviatoric tensor
LΔT	low ΔT (cycle)
m	time exponent in Norton–Bailey law (Eq. (4))
n	stress exponent in Norton–Bailey law (Eq. (4))
N, $N_{2\%}$	number of cycles, number of cycles to 2% load drop (crack initiation)
q_1	exponent in exponential term of Norton–Bailey law (Eq. (4))
t	time
T, T_{max}, T_{min}	temperature, maximum temperature, minimum temperature
TMF	thermo-mechanical fatigue
u	displacement (e.g. u_2^B, where subscript defines direction of action, i.e. '2' is axial, and superscript defines position, i.e. boundary plane or node number)
X	back stress tensor in Eq. (1)
Z	evolutionary softening factor, see Mazza et al. (2004b)

Greek letters

β	constant in exponential term of Norton–Bailey law (Eq. (4))
ε, $\bar{\varepsilon}$	strain, von Mises strain
$\Delta\varepsilon$	strain range
ε_e, ε_p, ε_c, ε_t	elastic strain, plastic strain, creep strain, total strain (these symbols with an overhead bar denote von Mises strains, i.e. $\bar{\varepsilon}_e$, $\bar{\varepsilon}_p$, $\bar{\varepsilon}_c$, $\bar{\varepsilon}_t$)
$\dot{\varepsilon}_p$	plastic strain rate
ε_{mean}	mean strain
ε_{mech}	mechanical strain
κ	control parameter (Eq. (5))
γ	exponent in yield function (Eq. (3))
σ, $\boldsymbol{\sigma}$	stress, stress tensor (Eq. (1))
σ_1, $\bar{\sigma}$, σ_m	maximum principal stress, von Mises stress, hydrostatic stress

qualify the deformation and endurance data gathered in terms of their practical applicability.

The following paper examines the results from a more recent test campaign conducted to examine the effect of varying the magnitude of the thermal transient in the TMF cycle on deformation and endurance characteristics. The evidence of physical damage accumulated during test by the specimens in this campaign is considered with reference to output from detailed finite element simulations of the series of TMF experiments.

Table 1
Material details

C (%)	Cr (%)	Mo (%)	Ni (%)	V (%)	$R_{p0.2}$ (MPa)	R_m (MPa)
0.25	0.88	0.76	0.69	0.33	660	803

2. Testing details

2.1. Material

The tests were performed on material taken from close to the surface of a 1CrMoV turbine rotor production forging. The chemical composition and room temperature tensile properties of the steel are summarised in Table 1. The forging had been oil quenched from 950/970 °C and tempered at 695/700 °C. The test material exhibited a mid-to-upper bainitic microstructure typical of large production forgings manufactured in this class of creep resistant low alloy ferritic steels.

2.2. Service-cycle TMF tests

Service-cycle TMF tests were performed on uniaxial tensile testpieces having a gauge section with a gauge section diameter of 12.7 mm and a gauge length of 12.7 mm (Fig. 2).

Three types of TMF cycle were investigated. Common to each were the detail of the mechanical strain cycle, with $\Delta\varepsilon_{mech}$ equal to 1.4%, and the maximum temperature in the thermal cycle of 565 °C (Fig. 3).[2] The superimposed temperature transients between T_{min} and 565 °C resulted in TMF cycles which had both in-phase and out-of-phase components. Intended to simulate a range of turbine start conditions, ΔT for the three cycle types was, respectively (a) 210 °C (LΔT), (b) 420 °C (IΔT) or (c) 520 °C (HΔT).

For the three cycle types, the mechanical strain was ramped from −0.2 to −1.6%, held at −1.6%, and then ramped to −0.4%, while the temperature was increased from T_{min} to 565 °C (Fig. 3). The time to 565 °C was 50 min, after which there was a hold time of 60 min at 565 °C. The mechanical strain was then increased from −0.4 to −0.2% as the temperature was reduced from 565 to 530 °C, and held at −0.2% as the temperature was returned to T_{min}.

In these TMF tests, particular attention was paid to the control of temperature gradient along the testpiece gauge length, and a limit of ±2 °C was maintained. Relatively high levels of geometrical instability had been experienced in earlier service-cycle TMF tests in which the temperature gradient had been typically ∼±5.5 °C, Holdsworth et al. (2004). While this was high, it conformed to the limit of max[$\pm 0.01 T_{max}$, ±3 °C] recommended in E 2368 (2004).

The results of the latest tests are summarised in Fig. 4. Increasing ΔT resulted in a reduction in cycles to crack initiation endurance (i.e. the number of cycles to a 2% drop in maximum load). Cycles to crack initiation ($N_{2\%}$) appeared to be

[2] A key to the symbols and terms used in the paper is given in the nomenclature section.

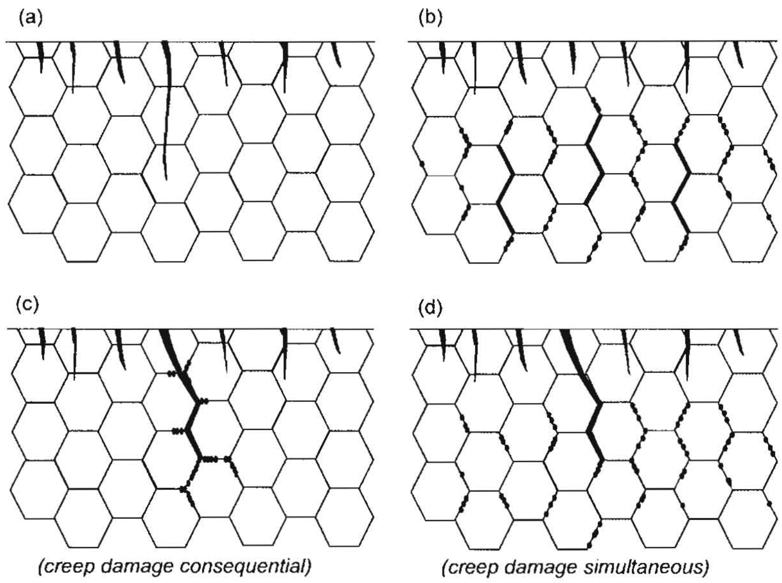

Fig. 1. Creep-fatigue failure mechanisms: (a) fatigue dominated, (b) creep dominated, (c) creep-fatigue interaction (due to consequential creep damage accumulation), and (d) creep-fatigue interaction (due to simultaneous creep damage accumulation).

relatively insensitive to thermal transients up to ~200 °C, but reduced with further increase in $T_{max} - T_{min}$.

3. Post test inspection

3.1. Dimensional instability

Following test, the specimens were inspected for evidence of dimensional instability and for creep-fatigue damage condition through the gauge section. The results of this evaluation are also summarised in Table 2. The maximum increase in gauge section diameter (Δd) occurred in the middle of the gauge length, and was of the order of 1.7% for the LΔT cycle testpiece at the end of life (Fig. 5), reducing to ~1.0% for the HΔT cycle testpieces.

The maximum reduction in gauge section diameter was observed towards the ends of the parallel length, and this was the order of −0.2% for the LΔT cycle testpiece at the end of life (Fig. 5), increasing to −1.3% for the HΔT cycle testpiece. Like the diameter increases observed at mid-gauge length, these Δd values are extremely small (the dimensional tolerance on the diameter is ±0.1%, see Fig. 2).

These dimensional changes are very low compared with previous experience with LΔT cycle tests for which temperature gradients were only restricted to within $\pm 0.01 T_{max}$, see Holdsworth et al. (2004). This evidence indicated a high level of dimensional stability in the latest series of TMF tests.

3.2. Damage development

Previous experience with this service-like TMF cycle was that creep and fatigue damage developed simultaneously during the course of test in the following way, Holdsworth et al. (2004). Fatigue cracking developed as a relatively uniform distribution of short transgranular cracks along and around the gauge section, ultimately to a depth of ~50 μm. In conditions for which cyclic loading was influential, ~1–2 dominant crack(s) propagated to much greater depth(s). At the same time, creep damage developed outwards from the axis and, typically in a more focussed

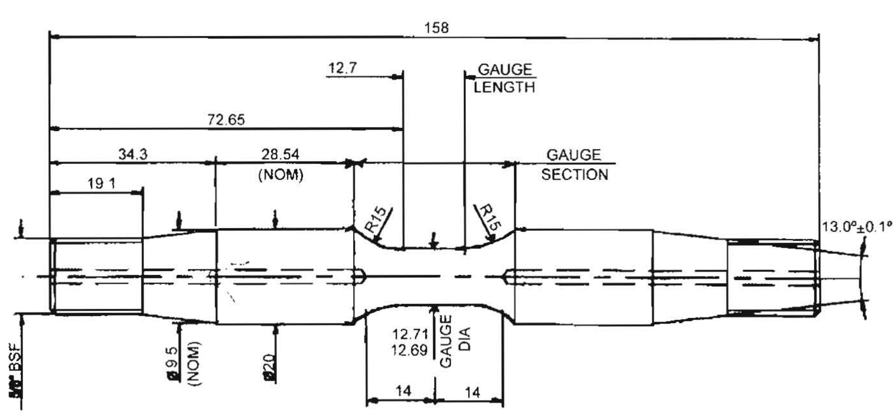

Fig. 2. TMF testpiece details (all dimensions in mm).

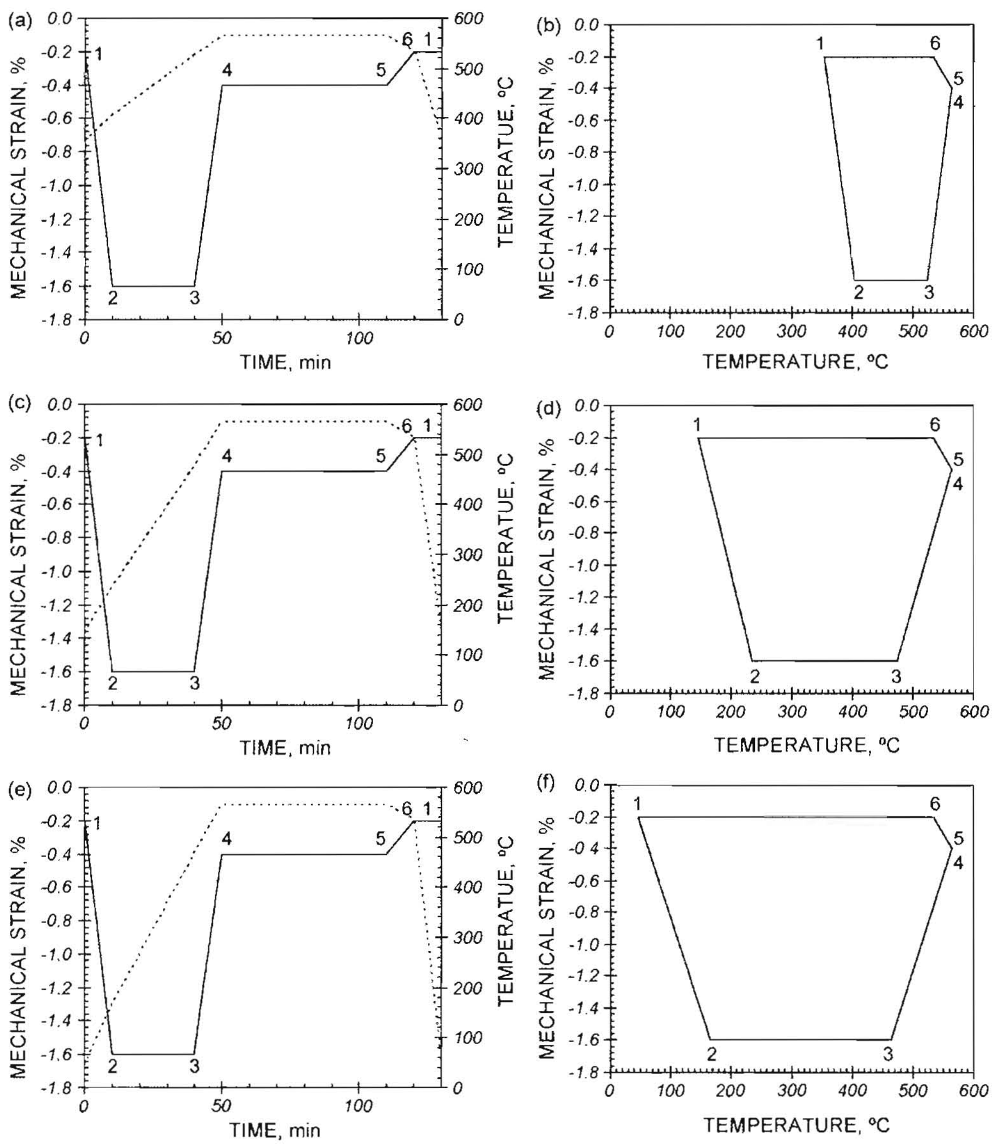

Fig. 3. Details of service-like TMF cycles: (a and b) LΔT cycle; (c and d) IΔT cycle; (e and f) HΔT cycle.

way, in the middle of the parallel length (Fig. 6a, inset). In the 1CrMoV steel, creep damage nucleated and coalesced at grain boundaries and propagated as intergranular cracking. Depending on the thermo-mechanical loading conditions, testpiece failure could be due to pure fatigue crack development from the surface, pure creep crack development from the axis, or creep-fatigue when a dominant fatigue crack interacted with the evolving creep damage zone, with the fracture path moving onto the grain boundaries (e.g. Fig. 1).

In the LΔT cycle testpiece of this testing campaign, the main crack initiated from close to one end of the parallel length of the gauge section (Fig. 5), but then propagated towards and into the region of advanced-condition creep damage evolving from the centre of the gauge section (Fig. 6a). The anticipated distribution of short fatigue cracks was evident at the surface. In addition, a crazed oxide appearance was apparent on the surface of the gauge length reflecting the enhanced rate of oxidation and oxide deformation arising from the imposed thermal and mechanical strain transients (Fig. 4).

Crack development in the IΔT cycle testpieces was creep dominated, with cracking propagating from the axis outwards (Fig. 6b). At the end of test there was a high intensity of relatively fine creep damage in the gauge section which appeared to be mainly located on grain boundaries in the form of coalesced cavity necklaces and microcracks. At the end of a duplicate test, it was possible to easily break open the specimen because of the loss of section arising from the intense fine distribution of creep damage. However, because all damage was sub-surface, the final fracture surface was completely unoxidised. There was reduced evidence of surface fatigue cracking in the IΔT cycle testpieces relative to that observed on the gauge length surface of the LΔT cycle testpiece (Fig. 6b). The extent of surface oxi-

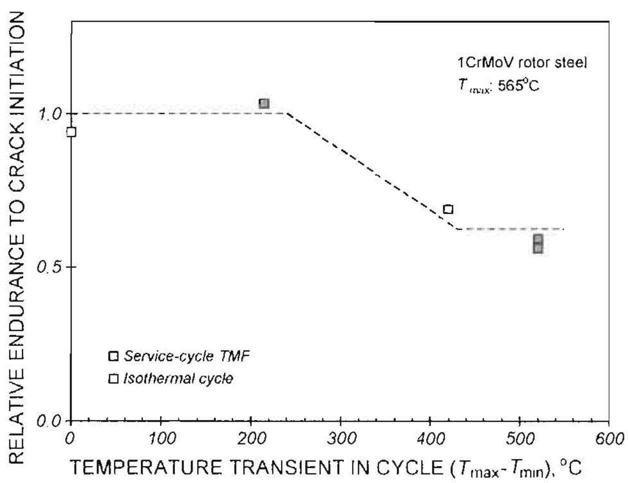

Fig. 4. Variation of endurance ($N_{2\%}$) with temperature transient in service-cycle TMF tests.

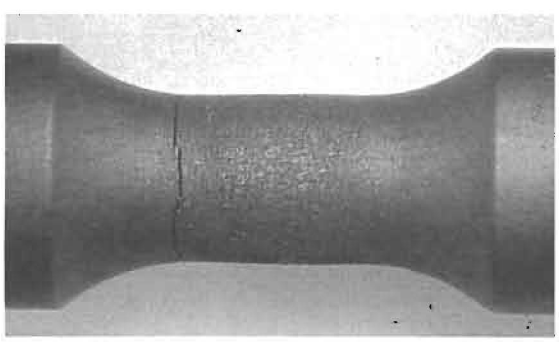

Fig. 5. Appearance of surface damage and cracking in gauge section of TMF testpiece.

dation, oxide crazing and spallation on the IΔT cycle testpieces was significantly greater than that observed on the LΔT cycle testpiece.

Crack development in the HΔT cycle testpieces was also creep dominated, with cracking propagating from the axis outwards (Fig. 6c). In all respects, the evidence was almost identical to that observed in the IΔT cycle testpieces, although in the HΔT cycle testpieces there was no indication of surface fatigue cracking. In the HΔT cycle tests, the extent of surface oxidation and spallation was so high due to the high thermal transient that the rate of metal removal at the surface appeared to be greater than the rate of short crack development.

4. State of stress/strain

4.1. Constitutive modelling

The states of stress and strain evolving in the testpieces during the course of TMF testing were analysed using the heat-specific non-unified constitutive model developed by Colombo et al. (2003) and Mazza et al. (2004b) for the 1CrMoV steel. The time independent plasticity term assumed non-linear kinematic hardening and isotropic softening in accordance with Lemaitre and Chaboche (1990). The yield criterion f and the evolutionary equation for the back stress tensor X are, respectively:

$$f = J_2(\sigma - X) = \sigma_0 Z \qquad (1)$$

$$\dot{X} = C\dot{\varepsilon}_p \frac{(\sigma - X)}{\sigma_0} - \gamma X \dot{\varepsilon}_p + \frac{1}{C} X \dot{C} \qquad (2)$$

where σ is the stress tensor, J_2 the second invariant of the deviatoric tensor, ε_p the equivalent plastic strain and Z is the evolutionary softening factor defined by Mazza et al. (2004b). The parameters σ_0, C and γ were determined from analytical fits to monotonic $\sigma(\varepsilon_p)$ tensile test records gathered at temperatures between 20 and 565 °C, Colombo et al. (2003), i.e. with:

$$\sigma_y = \frac{C}{\gamma}(1 - e^{-\gamma \varepsilon_p}) + \sigma_0 \qquad (3)$$

The time dependent plasticity model was based on the Norton–Bailey law, i.e.

$$\varepsilon_c = \beta e^{(-q_1/T)} A \left(\frac{\sigma}{Z}\right)^n \times t^m \qquad (4)$$

The equation set was implemented in finite-element simulations by means of a user-defined sub-routine in Abaqus. The

Table 2
Summary of results of post test inspection

Cycle	ΔT (°C)	Δd^{a} (%)	Observations
LΔT	210	+1.7, −0.2	Surface initiation close to end of parallel length (Fig. 5), with crack development to sub-surface creep damage concentrated in centre of parallel length (Fig. 6a) Significant evidence of short transgranular fatigue cracking at surface Enhanced gauge length oxidation, oxide crazing
IΔT	420	+1.4, −0.5	Main crack development from centre (Fig. 6b) Little evidence of short transgranular fatigue cracking at surface High level of gauge length oxidation/spallation
HΔT	520	+1.0, −1.3	Main crack development from centre (Fig. 6c) Little evidence of short transgranular fatigue cracking at surface Very high level of gauge length surface oxidation/spallation

[a] Δd is the local change in diameter at the end of test. The first figure given for each test is the measurement at the specimen mid-gauge length position (coincident with Node 11) while the second is the measurement at the extensometer leg position (coincident with Node 4), Fig. 7.

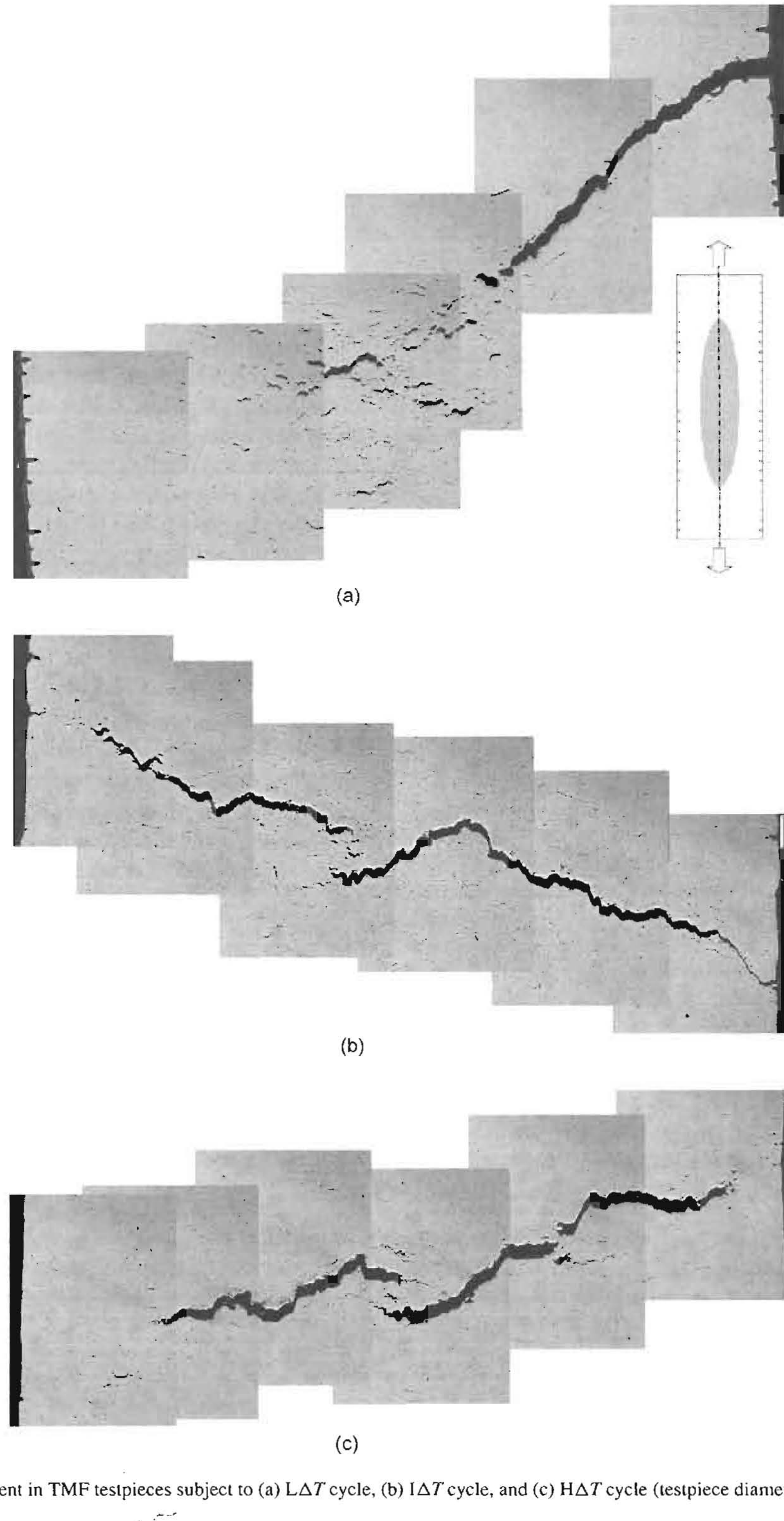

Fig. 6. Damage development in TMF testpieces subject to (a) LΔT cycle, (b) IΔT cycle, and (c) HΔT cycle (testpiece diameter is 12.7 mm in each case).

implementation included tabulations of σ_0, C and γ for specific temperatures in the range 20–575 °C. Cross reference to these enabled the temperature dependent implementation of Eqs. (1)–(3). The effectiveness of this implementation is considered in Sections 4.2 and 4.3.

4.2. Finite-element analysis

Non-linear finite-element calculations were performed in order to determine the through-section stress–strain response during the course of the TMF tests. The finite element model

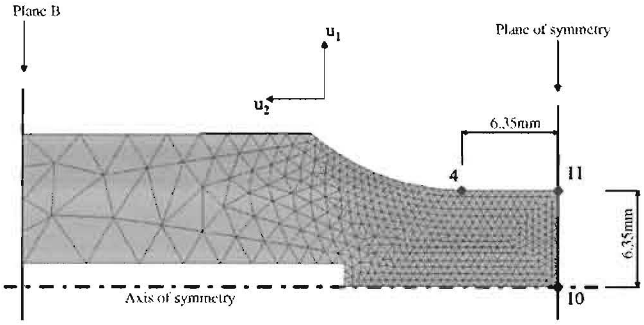

Fig. 7. Details of finite element mesh, with locations of Nodes 4, 10 and 11, and Plane B.

comprised an axisymmetric mesh with 6-node triangular elements, Fig. 7. The increment of axial displacement of nodes at plane B (i.e. Δu_2^B) was determined in each calculation step from the difference between the actual gauge length elongation (i.e. $u_2^4/6.35$ mm/mm) and the mechanical strain, required by the control profile of the cycle (Fig. 2), i.e.

$$\Delta u_2^B = \kappa\left(\frac{u_2^4}{6.35} - \varepsilon_{\text{mech}}\right) \tag{5}$$

The kinematic boundary conditions determined by Eq. (5) were calculated and also applied by means of a user-defined sub-routine in Abaqus. In this way, actual test conditions were reproduced in the simulation, with (i) axial displacement imposed remotely (at the grips), and (ii) its magnitude set to match the predefined gauge length elongation control profile. The approach enabled the cyclic progression of the (inhomogeneous) stress and strain state distribution within the testpieces to be simulated and analysed.

The ability of the Abaqus implementation of this constitutive model to represent the anisothermal cyclic stress–strain response of 1CrMoV steel has been demonstrated elsewhere by Colombo et al. (2003) and Mazza et al. (2004b). An additional indication of the effectiveness of the simulation was gained by comparing the FEA predicted local percentage Δd values for Node 11 (i.e. $u_1^{11}/6.35$) and Node 4 (i.e. $u_1^4/6.35$), given in Table 3, with the equivalent directly measured values at the specimen mid gauge length and extensometer leg positions (Table 2). Finite element analysis correctly predicted minor bulging at the mid-length position (Node 11) and minor necking at the extensometer leg position (Node 4), Fig. 7. It also predicted the tendency for increasing necking with increasing temperature transient (decreasing $T_{\min}$).

4.3. Stress–strain response

The results of the finite element simulations are compared with the measured nominal gauge-section stress–strain responses in Fig. 8. The good agreement between analytically determined and directly measured stress–strain response characteristics provided further evidence of the effectiveness of the Abaqus implementation of the constitutive model equation set (Eqs. (1)–(4)).

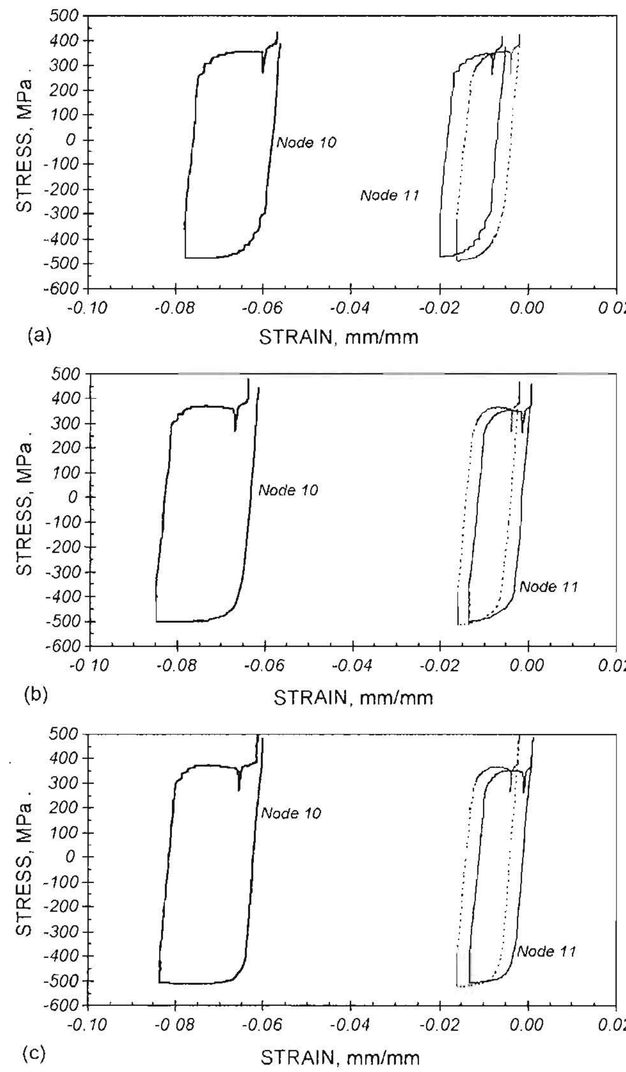

Fig. 8. FEA predicted local ratchetting at mid-life cycles of local stress–strain response at axis (Node 10, thick continuous loops) relative to local stress–strain response at surface (Node 11, thin continuous loops) and measured nominal gauge-section stress–strain response (thin dotted loops), for (a) LΔT cycle, (b) IΔT cycle, and (c) HΔT cycle.

The finite-element simulations highlighted significant differences between the local stress–strain responses generated at the surface and the axis in the middle of the parallel length of the TMF testpieces. For example, by mid-life ($0.5N_{2\%}$), significant ratchetting had displaced the local stress–strain responses at the axis (Node 10) from those at the surface (Node 11). For each cycle type, ratchetting was into compression at the axis (Fig. 8). The observed shifts are quantified in terms of mean strain in Table 3. The local axial mean strain at Node 10 is substantially shifted into compression with respect to the nominal $\varepsilon_{\text{mean}}$ value (i.e. from −0.90 to circa. −7%), with the shift increasing for increasing ΔT. In addition, the local axial strain range at Node 10 is ~50% higher than at the surface (Node 11) and its magnitude increases with change in cycle type from LΔT to HΔT (i.e. with increasing ΔT).

Table 3
Summary of finite element analysis predictions for $N = N_{2\%}$

Parameter	Units	LΔT cycle		IΔT cycle		HΔT cycle	
		Surface[a]	Axis	Surface	Axis	Surface	Axis
Δd^{b}	%	+2.08, −1.80		+2.74, −2.61		+2.60, −2.50	
$\Delta\bar{\varepsilon}_t{}^{c}$	%	1.39	2.17	1.43	2.35	1.43	2.36
$\bar{\varepsilon}_{mean}{}^{c}$	%	−1.29	−6.74	−0.64	−7.31	−0.60	−7.25
$\sum_0^{N_{2\%}} \bar{\varepsilon}_e{}^{d}$	%	+0.19	+0.19	+0.19	+0.20	+0.19	+0.20
$\sum_0^{N_{2\%}} \bar{\varepsilon}_p{}^{d}$	%	−70.61	−130.89	−47.83	−106.17	−38.60	−90.13
$\sum_0^{N_{2\%}} \bar{\varepsilon}_c{}^{d}$	%	+68.86	+120.09	+47.66	+93.59	+38.86	+77.29
$\sum_0^{N_{2\%}} \bar{\varepsilon}_t{}^{d}$	%	−1.56	−10.61	+0.02	−12.39	+0.45	−12.64
$\sum_0^{N_{2\%}} \bar{\varepsilon}_p/N_{2\%}$	%/cycle	−0.43	−0.79	−0.44	−0.97	−0.43	−1.00
$\sum_0^{N_{2\%}} \bar{\varepsilon}_c/N_{2\%}$	%/cycle	+0.42	+0.73	+0.43	+0.85	+0.43	+0.86
$\sigma_1/\bar{\sigma}^{e}$		+0.88	+1.04	+0.86	+1.03	+0.85	+1.04
$\sigma_m/\bar{\sigma}^{e}$		+0.22	+0.37	+0.20	+0.37	+0.20	+0.37
ΔT	°C	210		420		520	

[a] Surface data is generally at Node 11, and axial data is at Node 10 (Fig. 7), but see footnote b.
[b] The first figure in the Δd cells is that measured at the specimen mid-gauge length position (coincident with Node 11) while the second is that measured at the extensometer leg position (coincident with Node 4)—predictions for $N_{2\%}$.
[c] Local von Mises strain range and mean strain predictions at $0.5N_{2\%}$ (Fig. 8), cf. nominal (global) values of 1.40 and −0.90%, respectively.
[d] The tabulated accumulated (end of cycle) von Mises strains are for the respective $N_{2\%}$ cycles.
[e] The triaxiality ratios are those existing during the hold times of the respective mid-life ($0.5N_{2\%}$) cycles.

The local stress–strain response at the surface (Node 11) tended more into compression with respect to the nominal gauge-section stress–strain response during the course of the LΔT cycle test (Fig. 8a), but tended towards tension during the course of the IΔT and HΔT cycle tests (Fig. 8b and c respectively). The magnitude of these shifts is also quantified in terms of mean strain in Table 3. With respect to the nominal mean strain value (−0.90%), the local surface compressive ε_{mean} at Node 11 increases for the LΔT cycle, but progressively reduces in value for the IΔT and HΔT cycles. For all cycle types, the local surface strain range at Node 11 remains close to the nominal $\Delta\varepsilon_t$ value (1.4%), but at a marginally higher level.

The $N_{2\%}$ accumulated values of end-of-cycle elastic, plastic, creep and total strains local to mid parallel length surface (Node 11) and axial (Node 10) locations are summarised for the LΔT, IΔT and HΔT cycles, respectively, in Table 3. The local stress–strain response characteristics associated with each cycle type were a direct consequence of the way in which the respective components of inelastic strain accumulated. At the surface (Node 11), the calculated accumulated $-\bar{\varepsilon}_p$ and $+\bar{\varepsilon}_c$ components were almost balanced, with the higher magnitude compressive plastic strain components determining the respective shifts in mean strain for each cycle type. The magnitude of the $N_{2\%}$ accumulated inelastic strain components decreased with cycle type (LΔT to IΔT to HΔT) or increasing ΔT, due primarily to the reduction of $N_{2\%}$ with increasing ΔT (Table 3).

On the basis of previous experience, the dimensional instability observed in service-cycle TMF testpieces had been thought to be the inevitable consequence of such inhomogeneities in the gauge section stress–strain response. The evidence from this investigation indicated that inhomogeneous stress–strain fields do not always lead to dimensional instability.

The local $\sigma_1/\bar{\sigma}$ and $\sigma_m/\bar{\sigma}$ triaxiality ratios existing at the Nodes 11 and 10 positions during the 565 °C hold times were determined for each of the test types at the respective mid-life cycles. These are also summarised in Table 3. The local surface values were a little different to what was theoretically anticipated (i.e. 1.00 and 0.33) as a consequence of the internal stress state generated during cycling. The values at the axes were only marginally enhanced to indicate that the observed damage behaviour could not be attributed to high triaxiality.

5. Discussion

The results of a series of service-cycle TMF tests performed on a 1CrMoV steam turbine HP/IP rotor material and their analytical evaluation have revealed important observations about the development of thermal fatigue damage in this low alloy ferritic steel. Tests were performed using three TMF cycle types which differed only in the minimum temperature during the thermal transient (Fig. 3). In all other respects, the cycles were identical, having the same low ramp rate mechanical strain cycle in compression with a 1 h hold time at T_{max} of 565 °C. Increasing ΔT from 210 to 520 °C led to a reduction in the $N_{2\%}$ endurances (cycles to crack initiation), Fig. 4. If the accumulation of damage resulting from the thermo-mechanical cycle had been fatigue dominated (e.g. Fig. 1a) and the consequence only of cyclic plastic strain, the reverse trend could have been anticipated. High strain fatigue endurances tend to increase with decreasing temperature and therefore a reasonable expectation would be for the test cycle with the lowest average temperature to result in the highest number of cycles to crack initiation. However, damage development in these TMF testpieces is not fatigue dominated.

Physical damage development in the LΔT cycle testpiece is by creep-fatigue interaction (due to simultaneous creep damage accumulation, shown schematically in Fig. 1d), Fig. 6a. In contrast, damage development in the IΔT and HΔT cycle tests is creep dominated (Fig. 6b and c). The significant accumulation of creep damage from the axes of these TMF testpieces is the main factor contributing to the observed reduction in cycles to crack initiation with increasing ΔT.

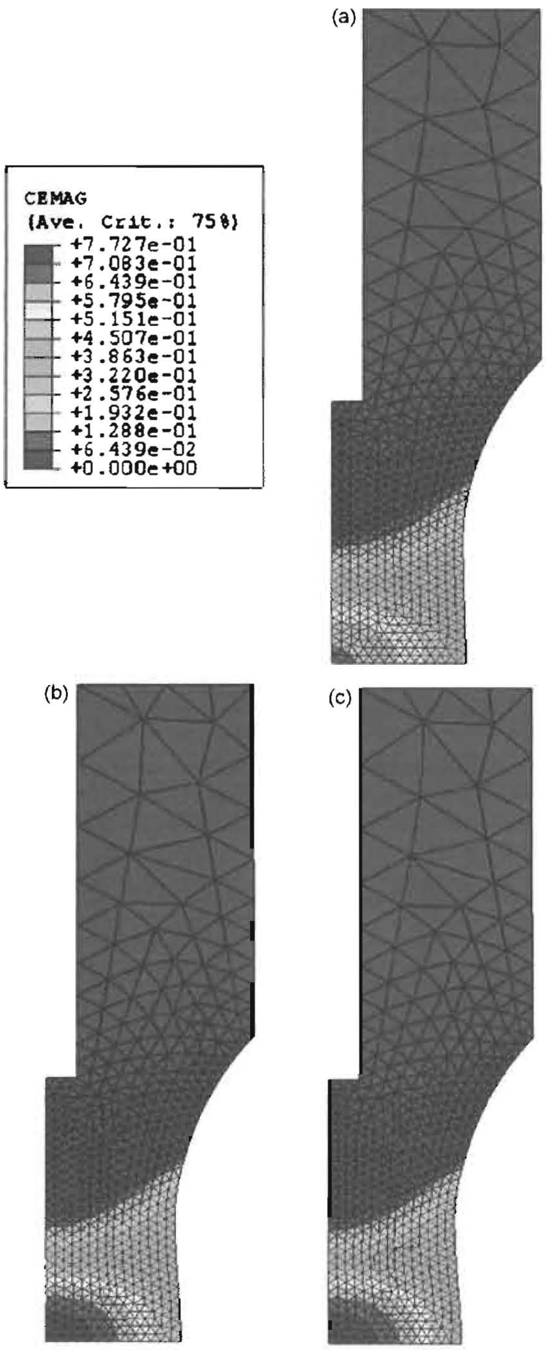

Fig. 9. Maps of FEA predicted cumulated equivalent creep strain at crack initiation after $N = N_{2\%}$ for HΔT cycle in TMF testpieces subject to (a) LΔT cycles, (b) IΔT cycles, and (c) HΔT cycles.

Finite element analysis predicts the generation of significant creep strains at the axes of the TMF specimens, at the end of test, with the largest strain accumulation arising in the LΔT cycle test and the lowest in the HΔT cycle test (Table 3). However, the rate of creep strain accumulation is lowest at the centre of the LΔT cycle specimen and similarly high at the centres of the IΔT and HΔT cycle specimens (Table 3). A comparison of the creep strains accumulated at testpiece centres after $N = N_{2\%}$ for the HΔT cycle test indicates that overall creep strain accumulation in the IΔT and HΔT cycle specimens is significantly higher than that in the LΔT cycle specimen after this number of cycles (Fig. 9).

In addition to the rates of creep strain accumulation being highest in the IΔT and HΔT cycle specimen tests, the oxidation/spallation rates are also observed to be significantly higher in the high thermal transient tests (Table 2). The evidence indicates that the rate of oxidation/spallation increased so much with increasing ΔT that the consequent rate of metal removal at the surface tended to exceed the rate of short crack development at the surface for ΔT greater than ~400 °C. There is respectively little or no evidence of fatigue cracking at the surfaces of the IΔT and HΔT cycle testpieces, Fig. 6b and c (cf. Fig. 6a).

While the apparent absence of fatigue damage at the surface of the high thermal transient service-cycle TMF specimens is an interesting observation, the phenomenon does not strongly influence the minimum lifetime of such tests. The lowest resistance to thermal fatigue damage development occurs when the rate of creep damage accumulation below the surface exceeds the rate of fatigue crack development at the surface. Reducing the magnitude of the thermal transient (in these circumstances, by decreasing ΔT) only results in an increase in thermal fatigue endurance when the rate of fatigue crack development exceeds the rate of creep strain accumulation.

These observations highlight the importance of predicting thermal fatigue lifetimes with a methodology which independently assesses damage components due to creep and fatigue and considers any interaction by an appropriate damage summation procedure. The adoption of an approach which does not independently assess the possibility of thermal fatigue damage due to creep developing from a sub-surface location is likely to be non-conservative.

6. Conclusions

In uniaxial service cycle thermo-mechanical fatigue tests formulated to simulate a range of steam turbine start cycles to a maximum temperature of 565 °C, the number of cycles to crack initiation for a 1CrMoV rotor steel is highest in low ΔT cycle tests and lowest in high ΔT cycle tests.

For these TMF cycles, the associated thermal fatigue damage mechanisms for the low alloy creep resistant steel are creep-fatigue interaction in low ΔT cycle tests and creep dominated in intermediate and high ΔT cycle tests.

Finite element analysis indicates that, with increasing cycle number, the local stress–strain response at the axis of service-cycle TMF testpieces is increasingly displaced into compression with respect to that at the surface; the magnitude of this displacement being highest for the high ΔT cycle tests. In addition, the local axial strain range at the axis is ~50% higher than at the surface, and is also highest for the high ΔT cycle tests. The dimensional instability associated with these local differences in stress–strain response is not significant.

The lowest resistance to thermal fatigue damage development occurs in the service-cycle TMF tests on 1CrMoV steel when the rate of creep damage accumulation below the surface exceeds the rate of fatigue crack development at the surface. Reducing the magnitude of the thermal transient only results in an increase in thermal fatigue endurance when the rate of fatigue crack development exceeds the rate of creep strain accumulation.

Acknowledgement

The authors acknowledge ALSTOM Power for supporting the work and for giving their permission to publish.

References

ASTM E2368, 2004. Standard practice for strain controlled thermomechanical fatigue testing, ASTM Standards, Section 3, vol. 03.01.

Bhongbhibhat, S., 1979. Untersuchungen über das Werkstoffverhalten in Gebiet der Zeitfestigkeit zur Erstellung von Berechnungsunterlagen für überwiegend thermisch beanspruchte Bauteille, Techn.-wiss. Ber. MPA Stuttgart, Heft 79-02.

Bicego, V., Fossati, C., Ragazzoni, S., 1988. Low cycle fatigue characterisation of a HP-IP steam turbine rotor, In: H.O. Solomon et al. (eds.), Low Cycle Fatigue, ASTM STP 942, Philadelphia, pp.1237–1260.

Colombo, F., Masserey, B., Mazza, E., Holdsworth, S.R., 2003. Simple modelling of the constitutive behaviour of a 1%CrMoV rotor steel in service-like thermo-mechanical fatigue tests. Mater. High Temp. 19 (4), 225–234.

Dawson, R.A.T., 1989. Monitoring and control of thermal stress and component life expenditure in steam turbines. In: Proceedings of the International Conference on Modern Power Stations, AIM, Liège.

Härkegard, G., 1992. Designing steam turbines for transient loading. In: Larsson, L.H. (Ed.), High Temperature Structural Design, ESIS 12. Mechanical Engineering Publications, London, pp. 21–40.

Holdsworth, S.R., 1996, Prediction of creep-fatigue behaviour at stress concentrations in 1CrMoV rotor steel. Proc. Conf. on Life Assessment and Life Extension of Engineering Plant, Structures and Components, Churchill College, Cambridge, September, 137-146.

Holdsworth, S.R., Mazza, E., Jung, A., 2004. The response of 1CrMoV rotor steel to service-cycle thermo-mechanical fatigue testing. ASTM J. Test Eval., 255–261.

Lemaitre, J., Chaboche, J.-L., 1990. Mechanics of Solid Materials. Cambridge University Press.

Masserey, B., Colombo, F., Mazza, E., Holdsworth, S.R., 2003. Endurance analysis of a 1%CrMoV rotor steel in service-like thermo-mechanical fatigue tests. Fatigue Fract. Eng. Mater. Struct. 26, 1041–1052.

Mayer, K.-H., Tremmel, D., 1979. The thermal fatigue of components in steam power plant. In: Proceedings of the International Symposium on Low Cycle Fatigue Strength and Elasto-plastic Behaviour of Materials, Stuttgart, October 8–9, 1979, pp. 105–116.

Mazza, E., Holdsworth, S.R., Skelton, R.P., 2004a. Characterisation of the creep-fatigue behaviour of a 1CrMoV rotor steel. Mater. High Temp. 21 (3), 119–128.

Mazza, E., Hollenstein, M., Holdsworth, S.R., Skelton, R.P., 2004b. Notched specimen thermo-mechanical fatigue of a 1CrMoV rotor steel. Nucl. Eng. Des. 234, 11–24.

Miller, D., Priest, R.H., Ellison, E.G., 1984. A review of material response and life prediction techniques under fatigue-creep loading conditions. High Temp. Mater. Process. 6 (3,4), 155–194.

Thomas, G., Dawson, R.A.T., 1980. The effect of dwell period and cycle type on high strain fatigue properties of 1CrMoV rotor forgings at 500–550 °C, Proceedings of the International Conference on Engineering Aspects of Creep, Sheffield, Paper C335/80.

Timo, D.P., 1969. Designing turbine components for low-cycle fatigue. In: Proceedings of the International Conference on Thermal Stresses and Fatigue, Berkeley, UK, September 22–26, 1969, pp. 453–469.